

525714
16P

NASA
SI-34
40264
N92-11118
p-13

A DETAILED INVESTIGATION OF STAGED NORMAL INJECTION INTO A MACH 2 FLOW

Dean R. Eklund
National Research Council, Hampton, Virginia
G. Burton Northam
NASA Langley Research Center, Hampton, Virginia
Roy J. Hartfield, Jr.
University of Virginia, Charlottesville, Virginia

ABSTRACT

A study of the staged injection of two jets of air behind a rearward facing step into a Mach 2 flow has been performed using the SPARK three-dimensional Navier-Stokes code. Calculated mole fraction distributions have been compared with an extensive set of planar mole fraction measurements made with a Laser-Induced Iodine Fluorescence technique. A statistical measure, the standard deviation, was used to help assess agreement between calculation and experiment. Overall, good agreement was found between calculated and measured values. Generally, agreement was better in the far field of the injectors. The effect of grid resolution was investigated by calculating solutions on grids of 60,000 points, 200,000 points and 450,000 points. Differences in the solutions on the two finer grids were small. However, the mole fraction distributions were distinguishable. The effect of turbulence modeling was investigated by employing three different algebraic models for the jet turbulence: the Baldwin-Lomax model, the Prandtl mixing length model and the Eggers mixing length model. Overall, the Eggers mixing length model was found to be superior for this case. Finally, the effect of the jet exit conditions was examined. A recently proposed Mach number distribution at the jet exit was found to improve slightly agreement between measurement and calculation.

INTRODUCTION

Success in developing viable propulsion systems for advanced vehicle concepts, such as the National Aero-Space Plane (NASP), will require that Computational Fluid Dynamics (CFD) play a strong role in support of ground and flight testing. Not only can CFD extend analyses to flight conditions beyond that which can be simulated on the ground, but also, numerical calculations provide detailed information that can assist engineers in understanding and interpreting experimental data. Before analysis based upon CFD calculations can be relied upon, however, the computer codes employed must be thoroughly calibrated. Recent work by Rudy et.al. [1] is representative of this endeavor. A critical step in code calibration is to model experiments that provide both reliable data and experimental conditions that can readily be simulated computationally.

Laser-Induced Iodine Fluorescence (LIIF) techniques have been developed at the University of Virginia for the experimental investigation of compressible flowfields. These nonintrusive optical techniques have been calibrated and provide detailed databases that can serve as benchmarks for CFD codes. These techniques have been used to investigate the staged normal injection behind a rearward facing step into a Mach 2 freestream. Earlier investigations yielded pressure and temperature measurements, but at a relatively sparse number of locations within the flowfield. These measurements have been useful, nevertheless, in previous

code validation studies (see, for example, References 2-3). Subsequently, much more extensive measurements have been taken. Measurements were taken of the pressure, temperature and velocity fields^[4] at over 350 locations and used to calibrate the SPARK Navier-Stokes Code. ^[5]

Recently, planar surveys of the injectant mole fraction have been taken using a planar LIIF technique^{[6],[7]}. Data have been taken at 35 crossflow stations and 4 streamwise stations with a resolution of 180x200 and 504x145, respectively. These data provide a truly extensive test for CFD codes and are used in a CFD code calibration effort for the first time in this paper. Due to the quantity of measurements taken, a statistical measure of agreement is used to aid analysis. The flowfield is modeled numerically using the SPARK code ^{[8],[9],[10]} developed at the NASA Langley Research Center. The computational effort in this work focuses on the effects of turbulence modeling and grid resolution. The effect of the conditions at the exit of the injectors is also examined.

This paper first describes the flowfield investigated. A brief description of the planar LIIF technique and the SPARK computer code then follow. Turbulence modeling is then examined, followed by details of the computational solution technique. Finally, comparisons between the computational and experimental results are examined and discussed, and conclusions are drawn.

FLOWFIELD

The flowfield analyzed in this work - the staged normal injection of two air jets behind a rearward facing step into a Mach 2 airflow - was investigated experimentally at the University of Virginia. This flowfield is depicted schematically in Figure 1 with the coordinate system indicated. (The origin of the coordinate system is at the first injector.) Specifically, flow with a stagnation pressure and temperature of 276 kPa and 303 K discharged from a Mach 2 nozzle into a test section that measured 21.285 mm in the normal direction and 29.21 mm in the spanwise direction (z and y , respectively). The step had a height of 3.175 mm and was located 11.02 mm downstream from the exit of the nozzle. The wall upstream of the step had a negative 0.5° slope to accommodate boundary layer growth. The circular jets measured 1.93 mm in diameter and were placed 3 and 7 step heights downstream of the step. The jets had a stagnation pressure and temperature of 266 kPa and 303 K. The measured mass flow rate of the injectors was approximately 1.63 g/s. The nominal exit Mach number was 1.35 which corresponds to a jet to freestream dynamic pressure ratio of 1.19. However, later measurements indicated that while the average Mach number is 1.35, there is a radial Mach number variation within the exit plane of the injector. The Mach number was found to vary from approximately 1.28 at the jet core to a Mach number of approximately 1.5 at the periphery of the jet.

The features of the flowfield are illustrated in Figure 1. After turning through an expansion fan centered at the step, the freestream near the centerline of the test section passes through two curved bow shocks formed by disturbances created by the two jets. Away from the centerline, the flow passes through a reattachment shock at a streamwise location near the first injector. The jets exhibit characteristic features of underexpanded jets - a barrel-shaped shock structure that the fluid expands into which is terminated by a normal shock wave, referred to as a Mach disk, that acts to equilibrate the pressure of the jet and the pressure of the main flow behind the bow shock. The second jet penetrates further than the first jet into the freestream due to the deflection of the freestream by the first jet. Downstream of the jets, a shear layer forms between the injectant and the freestream.

EXPERIMENTAL TECHNIQUE

The LIIF technique is a nonintrusive optical technique that infers flowfield properties from signals resulting from the laser-induced fluorescence of iodine molecules seeded into the flow. In general, laser-induced fluorescence involves the absorption and subsequent radiation of a photon by a molecule which has a transition that is resonant with the laser excitation wavelength. In a technique developed at the University of Virginia for making planar measurements of the injectant mole fraction, images of the time-integrated fluorescence signal are recorded using a charge coupled device camera. This provides a digitized record of the

fluorescence intensity at discrete locations within the flowfield. A ratio is taken between the signal obtained when only the injectant air is seeded and when the whole flow is seeded. The dependencies of the signal, due to the local thermodynamic properties of the air together with any dependencies due to the local laser intensity, cancel in the ratio. Hence, the ratio of the two signals provides a quantitative measure of the mole fraction at each location. A more detailed description of this technique and its application is given in References 6 and 7.

COMPUTER CODE

The computer code used in this study is one of the SPARK family of codes developed at the NASA Langley Research Center. The particular SPARK code employed solves the full three-dimensional unsteady Navier-Stokes equations together with appropriate species continuity equations. The combustion of H_2 and air is modeled with a 9-species 18-reaction chemistry model. In this work, however, a nonreacting flow is considered. The original code, developed by Drummond et.al.^{[8],[9]} solved the two-dimensional set of equations. This code was subsequently modified, by Carpenter^[10], to solve the three-dimensional set of equations while making efficient use of memory. This low memory version of the SPARK code provides two algorithms for solving the Navier-Stokes equations. The first algorithm is the original unsplit explicit technique of MacCormack which is a two-step predictor-corrector scheme. The algorithm is second-order accurate in both space and time. The second algorithm is the steady state Cross- MacCormack algorithm developed by Carpenter^[10]. This algorithm is accomplished by replacing the one-sided difference operators in MacCormack's predictor-corrector scheme with compact difference operators. The algorithm, while formally still second-order accurate in space and time, attains fourth-order spatial accuracy at steady state. Fourth-order artificial viscosity based on gradients of pressure and temperature is included in the solution algorithm to suppress numerical oscillations in the vicinity of shock waves.

TURBULENCE MODELING

The flowfield considered in this work is turbulent. While the turbulent fluctuations are not resolved, their effect upon the mean flow is modeled by solving the Reynolds-averaged conservation equations. These equations are obtained by first decomposing the fluid variables into mean and fluctuating components and then averaging over time. Because the conservation equations are nonlinear, averaging introduces additional unknowns: the Reynolds stresses, heat flux and mass flux terms, that represent the effect of the turbulent fluctuations upon the mean flow. A complete description of the Reynolds-averaged equations is beyond the scope of this paper. Further details can be found in Reference 11.

Most turbulence models calculate the turbulent stresses through the eddy viscosity (Bousinessq) approximation that relates the turbulent stresses to the mean rate of strain by a coefficient, called the eddy viscosity coefficient. This approximation assumes that the transport of fluid properties due to the motion of turbulent eddies is analogous to the molecular transport of fluid properties. Turbulence is then modeled as an increase in the transport coefficients, and the Reynolds-averaged equations using the eddy viscosity concept become equivalent to the instantaneous Navier-Stokes equations except for modifications to the transport coefficients. The effective transport coefficients take the form

$$\mu = \mu_l + \mu_t \quad (1)$$

$$k = C_p \frac{\mu_l}{Pr_l} + C_p \frac{\mu_t}{Pr_t} \quad (2)$$

$$\rho D = \frac{\mu_l}{Sc_l} + \frac{\mu_t}{Sc_t} \quad (3)$$

where μ , k , and D are the viscosity, thermal conductivity, and binary diffusion coefficients. ρ , Pr and Sc are the density, Prandtl and Schmidt numbers, and the subscripts l and t refer to the laminar and the turbulent components, respectively. Hence, turbulence is modeled through the eddy viscosity coefficient and the turbulent Prandtl and Schmidt numbers.

Analogous to molecular viscosity, the eddy viscosity coefficient is evaluated as

$$\mu_t = c\rho V L \quad (4)$$

where c is a constant, V is a velocity scale and L is a length scale. However, V and L are properties of the flow rather than properties of the fluid.

Only algebraic turbulence models, which evaluate the velocity and length scales from the mean flow, are considered in this work. The first model used for the staged jet flowfield is the Baldwin-Lomax model [12] which is used extensively for wall bounded flows, but also has been used with success for scramjet combustor flows. The Baldwin-Lomax model bases the velocity scale on the distribution of vorticity and the length scale on the distance from the wall.

The second model used combines the Baldwin-Lomax model along the walls with no effective turbulence modeling of the jet. This is achieved by limiting the search for the length scale in the Baldwin-Lomax model to the height of the boundary layer at the entrance to the test section. This model is referred to as the Laminar Jet model.

The third model combines the Baldwin-Lomax treatment of the wall boundaries as in the Laminar Jet model with a turbulence model for the jets based upon Prandtl's mixing length model. The eddy viscosity is defined as the maximum of the eddy viscosities calculated from the two models. This approach was used in Reference 13 to model the turbulence of a jet in a supersonic airflow. The constant in the model, as given in Reference 13, is 0.02. The length scale used in Prandtl's mixing length model is the average of the half-width of the jet in the spanwise and normal directions. The concentration of the injectant was used to determine the half-width. The velocity scale is defined as the maximum vorticity at a streamwise location times the mixing length. Additional details regarding the implementation of this model are found in Reference 5.

The fourth model combines the Baldwin-Lomax treatment of the wall boundaries, as above, with a turbulence model for the jets based upon Eggers' mixing length model which was designed for free shear layer flows as detailed in Reference 14. As implemented, this model is identical to the third model except for the constant and the velocity scale in the turbulence model for the jet. The velocity scale is defined as the velocity in the core of the jet, and the constant used is 0.0164 as given in Reference 14.

In all calculations the turbulent Schmidt and Prandtl numbers were set to constant values of .5 and .9, respectively. Riggins et.al. [15] noted that in the wake behind a bluff body and in the outer layer of a boundary layer it has been observed experimentally that the diffusion of mass is greater than the diffusion of momentum, thereby suggesting that the turbulent Schmidt number is less than unity in large portions of the near and far field of a normal injector. The turbulent viscosity was limited to 1,000 times the laminar viscosity in all calculations.

SOLUTION TECHNIQUE

Computational Grids

The grids used in the calculations were generated externally to the SPARK code using the exponential stretching functions found in Reference 16. Grid stretching is employed along the walls of the test section, in the vicinity of the step, and around the boundaries of the injectors. The effect of grid resolution has been investigated by increasing the resolution uniformly while keeping the stretching parameters constant.

To obtain accurate inflow conditions, calculations were made of the Mach 2 facility nozzle starting from the throat. The dimensions of the grids used in making calculations of the facility nozzle flowfield were 51x41 and 76x61. The minimum grid spacing at the wall at the exit of the nozzle was 55 and 35 microns,

respectively. The dimension of the grids used in the staged jet calculations were 69x41x21, 103x61x31 and 137x81x41. These grids will be referred to as Grids A, B and C, respectively. The domain extended 31 jet diameters downstream of the first injector. The minimum grid spacing at the base of the step in the normal direction was 80, 50 and 36 microns, respectively. The injectors were modeled with 13, 22 and 33 points, and the points were distributed to approximate a circular cross-section.

Boundary Conditions

The inflow boundary conditions for the nozzle calculation were determined from the tunnel reservoir conditions (assuming sonic, slug flow). Spline fits of pressure, temperature and velocity from the solution at the exit of the nozzle were then used as the inflow boundary conditions for the staged jet calculations.

Symmetry boundary conditions were applied by extrapolating from the adjacent station except for the normal velocity which was set equal to zero. Symmetry boundary conditions were invoked at the injector centerline plane.

Along solid walls, the no slip-condition was imposed together with assumptions of a zero normal pressure gradient, a zero normal total temperature gradient and a non-catalytic wall. However, the side tunnel wall was treated as an inviscid wall by setting the velocity at the wall equal in magnitude to the velocity at the adjacent station and in the direction of the wall while imposing a zero normal pressure gradient, a zero normal temperature gradient and a non-catalytic wall assumption. Neglecting to resolve the boundary layer on the side wall was not expected to appreciably affect the accuracy of the solution in the vicinity of the jets.

At the jet injection points the conditions were fixed from the reservoir values and an experimentally determined Mach number. The areas of the injectors were set so that the resulting mass flow rate matched the measured mass flow rate. The conditions at the corner of the step were obtained by bilinear extrapolation from the three adjacent points in the normal and streamwise directions. Finally, the flow variables along the outer boundary were extrapolated from the interior assuming a zero gradient.

Iteration Technique

Initial solutions were started by setting the flow quantities in the domain equal to their values at the inflow plane. However, behind the step a profile in velocity was assumed and the pressure at the jet exits was incremented gradually up to its experimental value. Course grid solutions were used as initial conditions for fine grid solutions. Similarly, a solution using one turbulence model was used as the initial condition for a solution using a second turbulence model.

The solutions were advanced in time using a local time step with a Courant number of 0.2, unless otherwise indicated. The local time step was calculated by combining the convective and the diffusive time scales [5]. The artificial viscosity coefficients were set equal to 0.5, unless otherwise indicated. A true steady state solution was not attained. Within the recirculation zones, the pressure was found to vary between 5 and 10 %. In many places within the recirculation zone the oscillations possessed a distinct periodicity. Consequently, convergence was assessed by visual inspection of mole fraction contour plots together with plots of mass conservation. When the contour and mass conservation plots showed relatively no change between successive runs, the calculation was continued for 2,000 iterations over which mean values were calculated. Overall, between 10,000 and 30,000 iterations were required to attain this convergence.

RESULTS AND DISCUSSION

Nozzle Flow

Calculations of the Mach 2 nozzle were made using the Baldwin-Lomax turbulence model, while assuming 2-dimensional flow. Solutions on the two grids (51x41 and 76x61) provided nearly identical profiles. A solution was also obtained assuming laminar flow. The turbulent solution more closely matched temperature measurements made across the duct (in the z-direction) .44 mm or .14 step heights upstream of the step. The calculated boundary layer thickness was approximately 1.62 mm or .51 step heights at the exit of the nozzle.

Staged Jet Flow

Unless otherwise indicated, the solutions discussed were obtained by assuming that the Mach number at the exit of the jets was uniform and equal to 1.35. The solution obtained with the Eggers turbulence model on Grid B will be referred to as the baseline case. Figure 2 shows the velocity vectors along the centerline plane (Figure 2A) along three crossflow planes (Figures 2B, 2C and 2D) and along a plane one-half step height above the base of the test section (Figure 2E) from the baseline solution. (The qualitative features were not strongly influenced by the grid density and the turbulence modeling.) The three arrows perpendicular to the x-axis in Figure 2A indicate the position of the three crossflow planes. The vortex generated by the second jet is depicted clearly in the crossflow plots. The 3-dimensional nature of the flowfield is illustrated by the streamlines in the centerline plane which do not fill in the area behind the injectors. This is accomplished by the vortices generated by the jets as shown in Figures 2B-E.

Because of the abundance of data - 35 crossflow planes and 4 streamwise planes representing a combined 1.55 million measurements- a statistical measure of agreement between experiment and calculation was desirable. Consequently, a standard deviation between measured and calculated values was calculated for each experimental plane. This was accomplished by using tri-linear interpolation to interpolate the calculated values to the experimental grid locations. That is, for each experimental point, the four computational grid points closest to the experimental point were determined and these four points were used to interpolate to the experimental location. The standard deviation was then obtained from the calculated and measured values according to

$$\sigma = \sqrt{\frac{\sum_{i=1}^N (e_i - c_i)^2}{N - 1}} \quad (5)$$

where σ is the standard deviation, e_i is the measured mole fraction at location i , c_i is the interpolated mole fraction obtained from the calculated solution, and N is the number of experimental locations. However, between different planes there is a widely varying proportion of points having a non-zero mole fraction, which would result in an artificially low value of σ in the near field of the injectors. To partially alleviate this effect σ was modified to

$$\sigma = \sqrt{\frac{\sum_{i=1}^N (e_i - c_i)^2}{NG3 - 1}} \quad (6)$$

where $NG3$ is the number of experimental points with a mole fraction greater than 3%. Other statistical measures that may be more appropriate will be investigated in the future.

The effect of the coarseness of the interpolation was investigated. Shown in Figures 3A and 3B are plots of the standard deviation calculated from the baseline case for the crossflow planes and the streamwise planes, respectively, while varying the resolution of the experimental data. That is, first the entire experimental domain was used to calculate σ (increment = 1, 180x200 grid for the crossflow planes) secondly every fourth experimental point was used (increment = 4, 45x50 grid for the crossflow planes) then every sixteenth

experimental point was used (increment = 16, 12x13 grid for the crossflow planes). There is little discernible difference in the calculated σ using every single and every fourth experimental point. (For the calculations of σ in this paper the entire experimental domain was used.) Consequently, the values of the standard deviation are not dependent on the number of experimental data points. Neither are they believed to depend on the accuracy of the interpolation used.

The standard deviation plots in Figure 3 reveal that the difference between the measured and calculated values is larger in the vicinity of the injectors where the gradients are large and decreases as one moves downstream. This trend is characteristic of all of the turbulent solutions obtained. Note that a standard deviation of 0.08 implies that the average difference between the experimental and the calculated mole fractions is no greater than 0.08. A comparison between selected contours from the baseline case and the LIIF data is shown in Figures 4 and 5. (For the mole fraction contour plots in this paper the interval between contour lines is 0.05.) Overall, the qualitative features of the mole fraction signatures are in accord. Nevertheless, the first crossflow plane ($x/d = -2$) indicates a smaller concentration of injectant in the recirculation zone in the calculated solution. At the first injector ($x/d = 0$) the profile of the jet is slightly taller and thinner in the calculated solution. This trend continues until approximately $x/d = 8$ (Figure 4D) where a strong vortex behind the second jet acts to lift the injectant away from the wall. This effect appears slightly more pronounced in the measurements. The bounding 0.05 contour line extends farther in the measurements beyond the $x/d = 8$ station. The maximum mole fraction in the calculated solution at each station is consistently larger than the maximum mole fraction measured by approximately 0.10. This difference is reduced in the far field as evidenced by the $x/d = 30$ crossflow station (Figure 4F) comparison where the difference in the maximum mole fraction is less than 0.05. Mole fraction comparisons at two streamwise planes are shown in Figure 5. Again good qualitative agreement is observed but overall the calculated solution exhibits greater mole fraction values.

The effect of grid resolution was studied by making calculations on Grids A, B, and C with the Eggers turbulence model. (The solution on Grid C was obtained with the CFL time step limit and the numerical viscosity coefficients equal to .1 and .6, respectively.) A standard deviation with respect to the solution obtained on Grid C, designated as σ_C , was obtained by interpolating each solution to the same domain and then calculating the standard deviation of the solution from grids A and B to the solution from grid C. This quantity was used to assess grid convergence and is plotted in Figure 6A. Note the sharp peak before and after the first injector and to a lesser extent before and after the second injector. This is likely due to the discretization of the injectors. Also note that the agreement is better between grids B and C than between grids A and C, as expected, and that the agreement between grids A and C is worse in the near field of the injectors where the gradients are more severe. Although differences in the solutions obtained on Grids B and C are discernible throughout the domain, the differences are relatively small. This result is in accord with an earlier study [5] which found little difference in the pressure, temperature and velocity values at most experimental locations for the solutions from grids B and C.

The standard deviation between the measured values and each of the three solutions is shown in Figure 6B. In the near field the solution from grid A is distinctly inferior to the solutions on the finer grids which was also observed in Reference 5. In the far field, the standard deviation is seen to decrease with downstream distance as noted earlier, however, perhaps surprisingly, the standard deviation is seen to increase with increasing grid resolution. This trend is thought to be an effect of numerical diffusion fortuitously compensating for the inaccuracies of the turbulence modeling. Numerical diffusion which smears gradients will act to diffuse the jet and reduce the mole fraction within the jet. Also, numerical diffusion decreases as the grid resolution increases. As previously noted, the calculated solutions have a greater mole fraction in the jet core than do the measurements. Hence, numerical diffusion will tend to bring the calculated mole fractions closer to the experimental values which explains why the standard deviation is lower in the far field for the coarser grid solution. Selected crossflow planes are shown in Figure 7 to illustrate further the effects of grid resolution. Generally, in the coarse grid solution, the profiles are not as well defined and the bounding 0.05 mole fraction contour extends farther in the normal direction.

Because the solutions on Grids B and C were relatively unchanged with the Eggers turbulence model,

the effect of turbulence modeling was investigated by obtaining solutions on Grid B with the Prandtl and the Baldwin-Lomax turbulence models. Also, a solution using the Laminar Jet model was obtained on Grid A. Plots of the standard deviation between the measurements and these solutions together with the Eggers turbulence model solution on Grid B are shown in Figure 8. In the near field the standard deviation from the Baldwin-Lomax and the Laminar Jet model solutions are elevated relative to the solutions obtained with the Eggers and the Prandtl models. In the far field the Baldwin-Lomax model solution is seen to attain similar standard deviation levels as the solutions using the Eggers and Prandtl models, while the Laminar Jet model solution maintains a high standard deviation. Contours of the ratio of the turbulent eddy viscosity to the laminar viscosity ^[5] indicate that the solution from the Baldwin-Lomax model is marked by an uneven distribution of eddy viscosity in the near field, which is not unexpected, since the length scale is based upon the distance from the wall. Also, regions of large eddy viscosity are relatively small in the near jet region. The eddy viscosity distributions from the solutions using the Prandtl and Eggers mixing length model more closely track the jet, as designed. Generally, the Prandtl model was found to yield the largest eddy viscosity values. The effects of the turbulent viscosity distributions are evident in the mole fraction contours as seen in Figures 9-10. The solutions using the Baldwin-Lomax model and the Laminar Jet model have similar profiles in the near field as evidenced in Figures 9A and B which is due to the small turbulent viscosity calculated by the Baldwin-Lomax model in this region. In the far field (Figures 9C and D) the Laminar Jet model solution illustrates the effect of zero turbulent diffusion. Without turbulence, the injectant jet core remains bifurcated at the last crossflow station ($x/d = 30$) unlike in the measurements and in the turbulent solutions (see Figures 4F and 10D). Also, there is little spreading as the vortex lifts the core towards the top wall. In Figure 10, the solution using the Prandtl mixing length model is compared to the measured values. The turbulent diffusion is greatest for the solution using the Prandtl model which corresponds to enhanced spreading and lower peak mole fraction values. Hence, the peak mole fraction values are closer to the peak measured values, however, the turbulent diffusion in the Prandtl model solution has obscured features of the mole fraction profiles as shown in the contour plots at the $x/d = 0$ and $x/d = 8$ streamwise locations (Figures 10A and B). Hence, overall, the Eggers mixing length model is judged to outperform the other turbulence models considered.

Finally, the effect of the conditions at the exit of the jet was investigated. Recent measurements indicate that the Mach number varies radially from 1.28 at the center of the jet to 1.5 at the edge of the jet with an average Mach number of 1.35. To test the effect of this variation a solution was obtained by letting the Mach number vary linearly from sonic at the center of the jet to 1.5 at the edge of the jet, but maintaining the original mass flow rate. Another solution was obtained by assuming sonic flow, and adjusting the injector area to maintain the same mass flow rate. Both of these solutions were calculated using Grid A and the Eggers turbulence model. The standard deviation to the measurements is shown in Figure 11. The effect is small, but favorable, especially for the solution with a Mach number distribution at the jet exit.

CONCLUDING REMARKS

Overall, good agreement was found between measurement and calculation. Generally, agreement was better in the far field of the injectors. The effect of grid resolution was investigated by calculating solutions on grids of 60,000 points, 200,000 points and 450,000 points. Differences in the solutions on the two finer grids were small. However, the mole fraction distributions were distinguishable. Surprisingly, in the far field, the effect of numerical diffusion caused the solution on the coarse grid to more closely approximate the measurements. The effect of turbulence modeling was investigated by calculating solutions with three different algebraic models for the jet turbulence. The solution obtained with the Baldwin-Lomax model was comparable to the solutions obtained with the Prandtl and the Eggers mixing length models in the far field, but it was clearly inferior in the near field. The solution calculated with the Prandtl mixing length model was slightly more favorable than the solution obtained with the Eggers mixing length model in the far field, but in the near field it was inferior and muted some of the prominent flow features. Hence, the Eggers mixing length model was judged superior among the turbulence models tested for this case. Finally, the effect of the jet exit conditions was examined. Varying the Mach number at the exit of the jet while maintaining the same mass flow rate was found to have a small effect upon the mole fraction distributions.

Nevertheless, a recently proposed Mach number distribution at the jet exit did slightly improve agreement between measurement and calculation.

References

- [1] Rudy, D. H.; Thomas, J. L.; Kumar, A.; Gnoffo, P. A.; Chakravarthy, S. R.: A Validation Study of Four Navier-Stokes Codes for High-Speed Flows. AIAA Paper No. 89-1838, June, 1989.
- [2] Uenishi, K.; Rogers, R. C.; and Northam, G. B.: Three-Dimensional Numerical Predictions of the Flow Behind a Rearward-Facing Step in a Supersonic Combustor. AIAA Paper No. 87-1962, June-July, 1987.
- [3] Rhie, C. M.; and Saadat, A. S.: Critical Evaluation of Three- Dimensional Supersonic Combustor Calculations. AIAA Paper No. 90-0207, January 1990.
- [4] Fletcher, D. G.; and McDaniel, J. C.: Quantitative Characterization of a Nonreacting, Supersonic Combustor Using Laser-Induced Iodine Fluorescence. AIAA Paper No. 89-2565, July 1988.
- [5] Eklund, D. R.; Northam, G. B.; and Fletcher, D. G.: A Validation Study of the SPARK Navier-Stokes Code for Nonreacting Scramjet Combustor Flowfields. AIAA Paper No. 90-2360, July 1990.
- [6] Hartfield, R. J.; Abbitt, J. D.; and McDaniel J. C.: Injectant Mole-Fraction Imaging in Compressible Mixing Flows Using Planar Laser- Induced Iodine Fluorescence. Optics Letters, Vol. 14, No. 16, August 15, 1989, pp. 850-852.
- [7] Hartfield, R. J.; Hollo, S. D.; and McDaniel J. C.: Planar Measurement of Flow Field Parameters in a Nonreacting Supersonic Combustor Using Laser-Induced Iodine Fluorescence. AIAA Paper No. 90-0162, January, 1990.
- [8] Drummond, J. P.; Rogers, R. Clayton; and Hussaini, M. Yousuff: A Detailed Numerical Model of a Supersonic Reacting Mixing Layer. AIAA Paper No. 86-1427, June 1986.
- [9] Drummond, J. P.; and Hussaini, M. Yousuff: Numerical Simulation of a Supersonic Reacting Mixing Layer. AIAA Paper No. 87-1325, June 1987.
- [10] Carpenter, M. H.: Three Dimensional Computations of Cross-Flow Injection and Combustion in a Supersonic Flow. AIAA Paper 89-1870, June 1989.
- [11] Rubesin, Morris W.; and Rose, William C.: The Turbulent Mean-Flow, Reynolds-Stress and Heat-Flux Equations in Mass-Averaged Dependent Variables. NASA TM X-62,248, 1973.
- [12] Baldwin, B. S.; and Lomax, H.: Thin Layer Approximation and Algebraic Model for Separated Turbulent Flows. AIAA Paper No. 78-257, Jan. 1978.
- [13] Chitsomboon, T.; Northam, G. B.; Rogers, R. C.; and Diskin, G. S.: CFD Prediction of the Reacting Flowfield Inside a Subscale Scramjet Combustor. AIAA Paper No. 88-3259, July 1988.
- [14] Eggers, James M.: Turbulent Mixing of Coaxial Compressible Hydrogen-Air Jets. NASA TN D-6487, 1971.
- [15] Riggins, D. W.; Mao, M.; Bittner, R. D.; McClinton, C. R.; and Rogers, R. C.: Numerical Modeling of Normal Fuel Injection: Effect of Turbulent Schmidt Number. NASP Report, Ref. WBS 2.4.09, March 1989.
- [16] Anderson, D. A.; Tannehill, J. C.; and Pletcher, R. H.: Computational Fluid Mechanics and Heat Transfer. McGraw-Hill, New York, 1984, pp. 247-251.

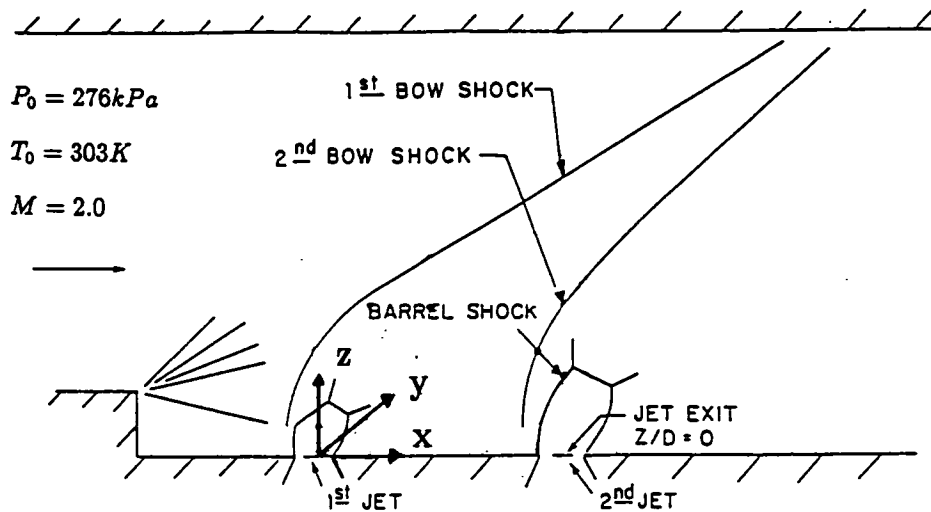


Figure 1. Schematic of the staged jet flowfield.

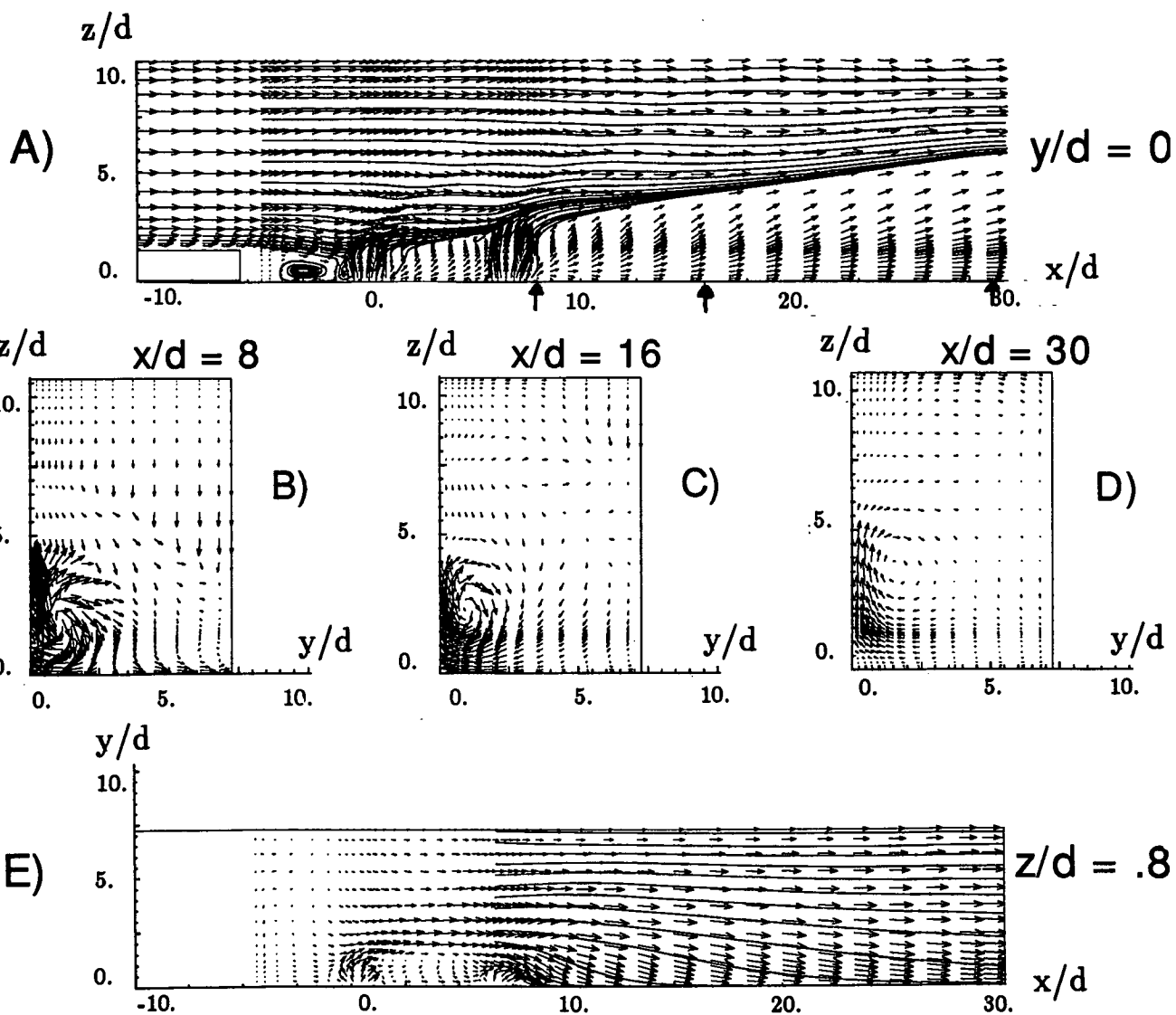


Figure 2. Velocity vector plots along five planes from the baseline solution.

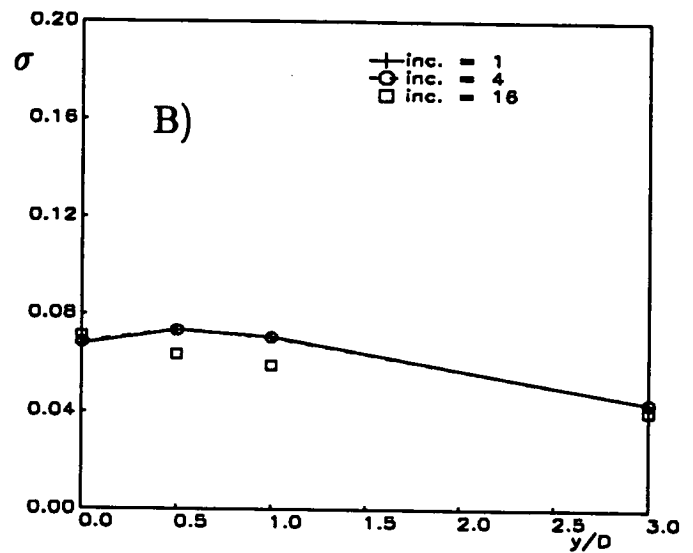
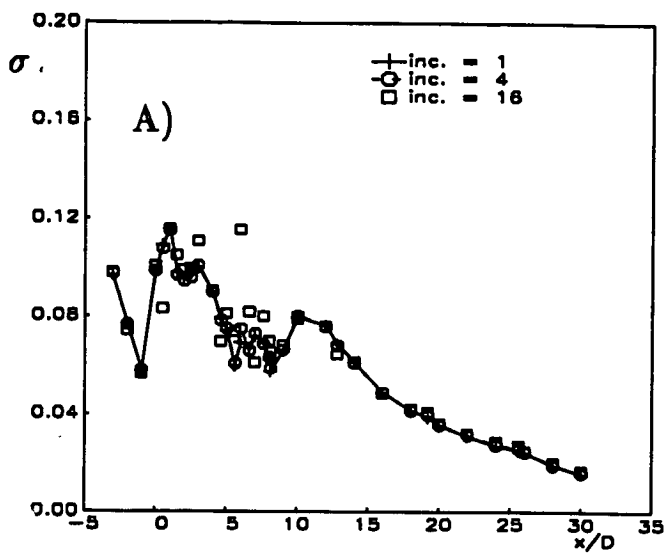


Figure 3. Standard deviation plots for different experimental grid resolutions.

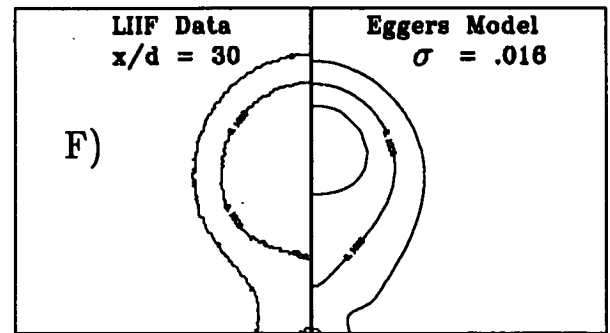
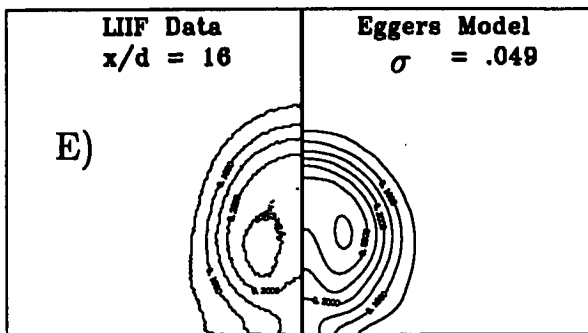
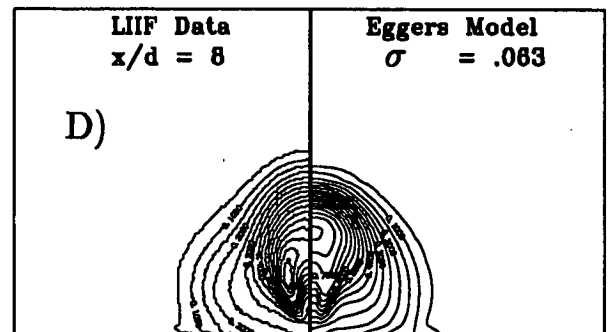
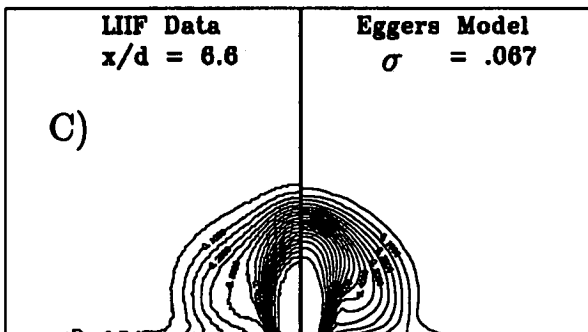
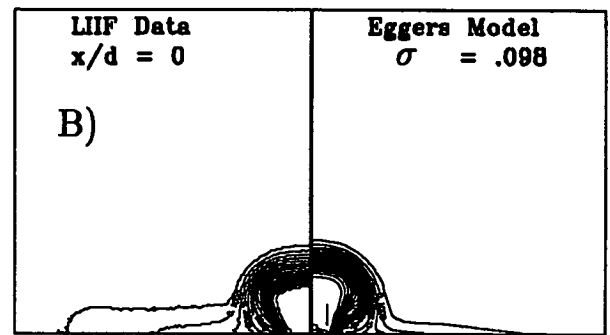
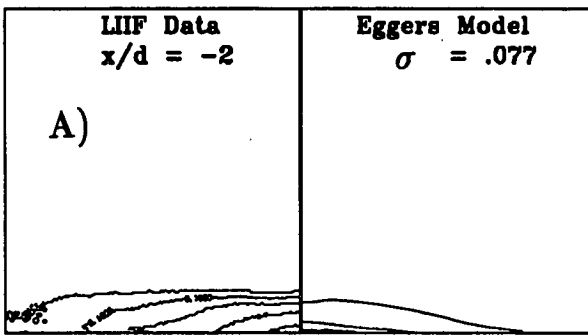


Figure 4. Comparison between the measured and the baseline mole fraction values at six crossflow planes.

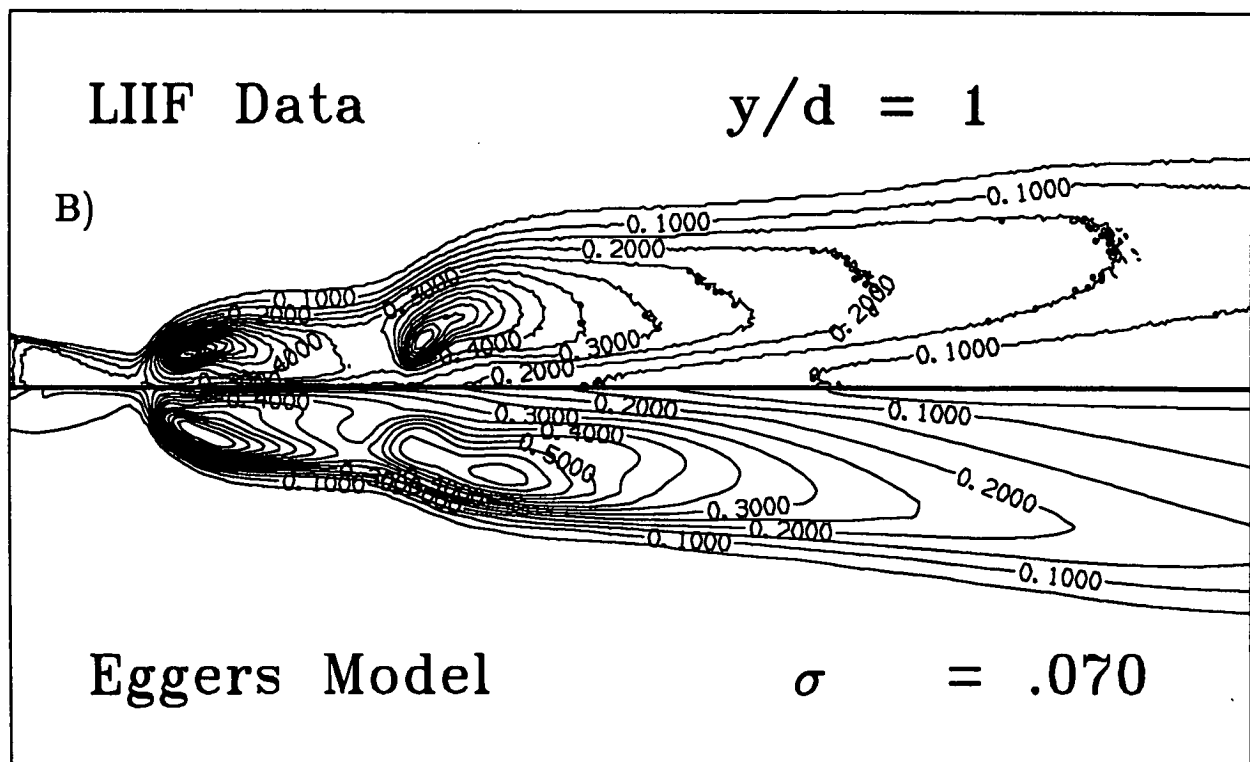
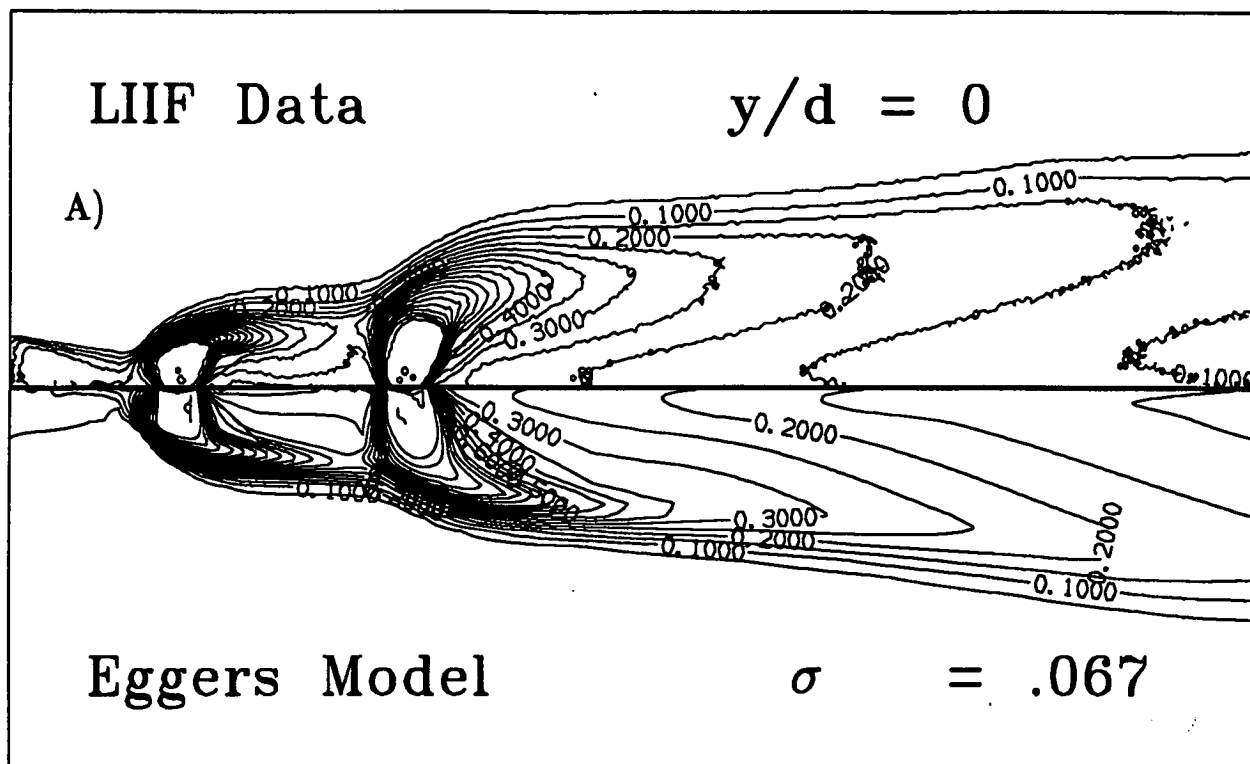


Figure 5. Comparison between the measured and the baseline mole fraction values at two streamwise planes.

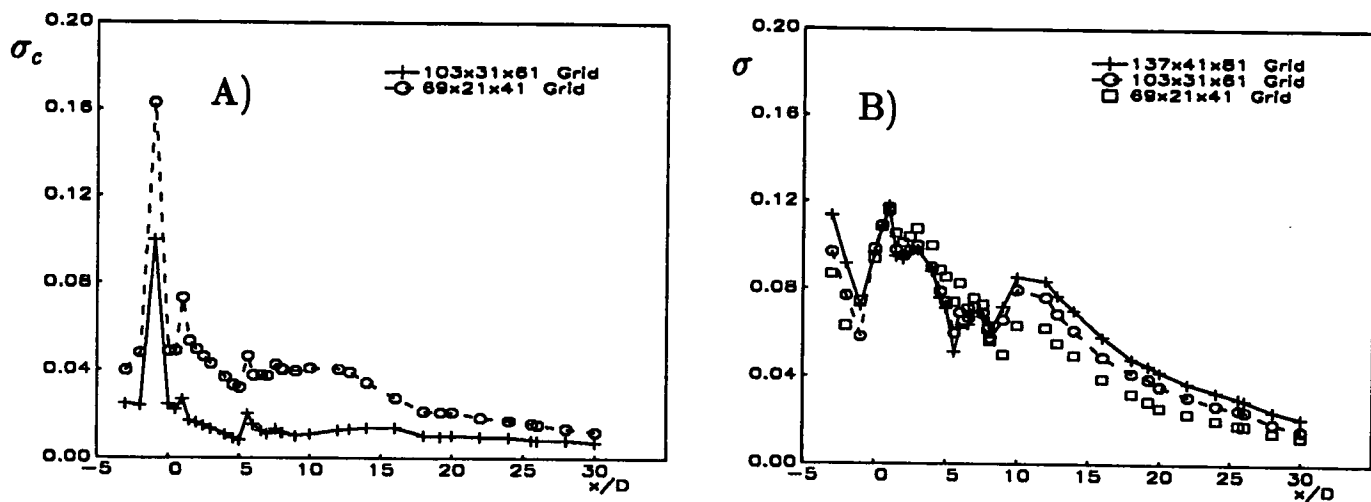


Figure 6. Standard deviation plots for solutions on different grids.

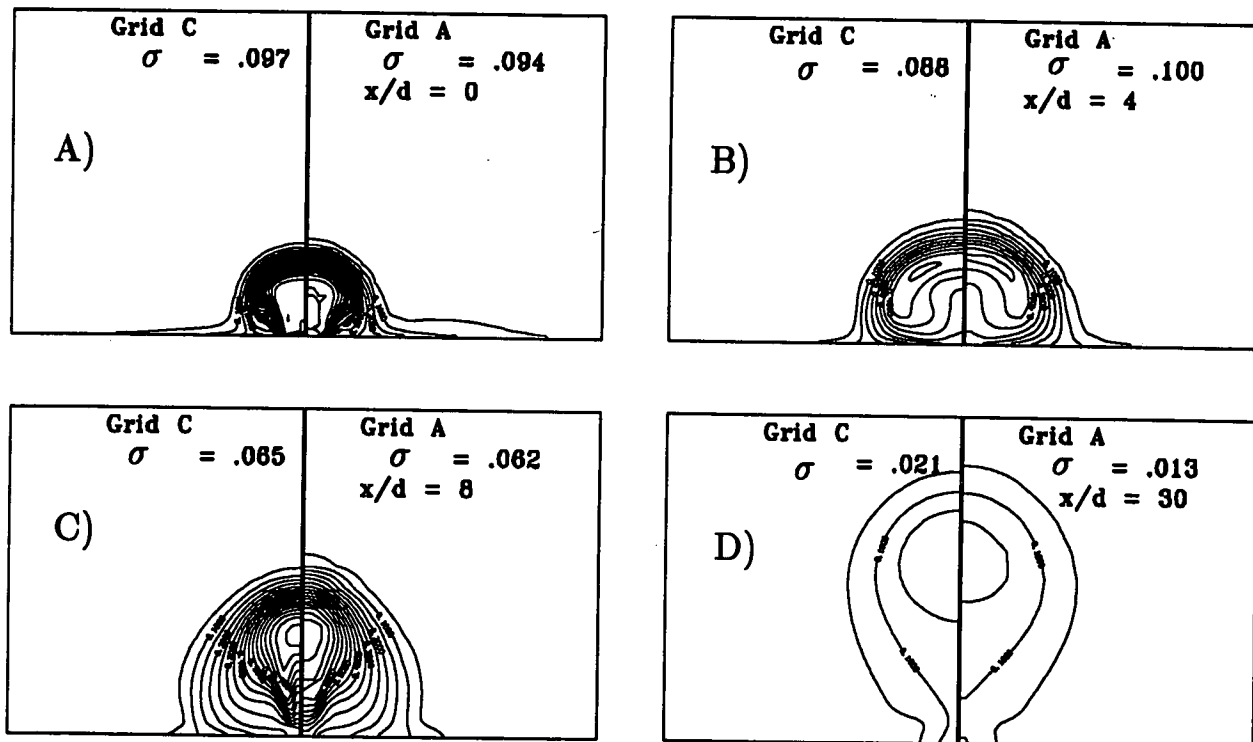


Figure 7. Comparison of mole fraction values at four crossflow planes between solutions on Grids A and C.

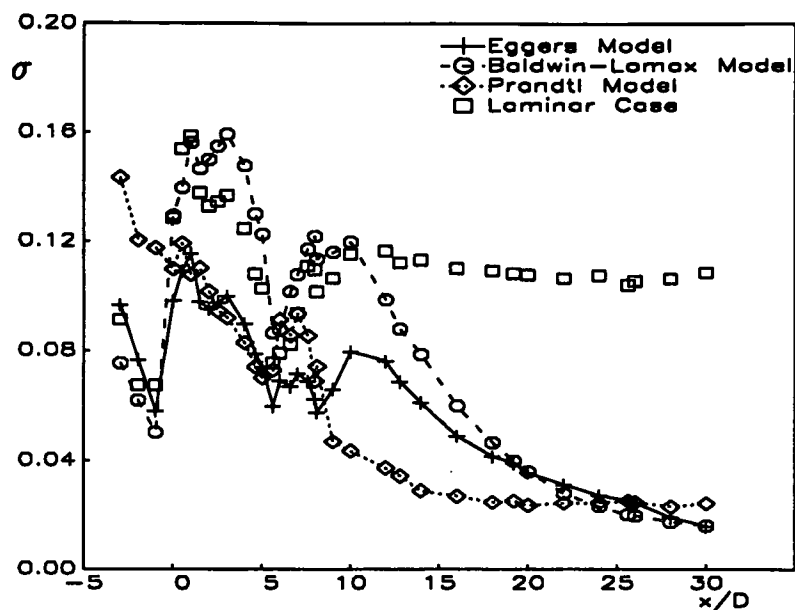


Figure 8. Standard deviation for solutions obtained with different turbulence models.

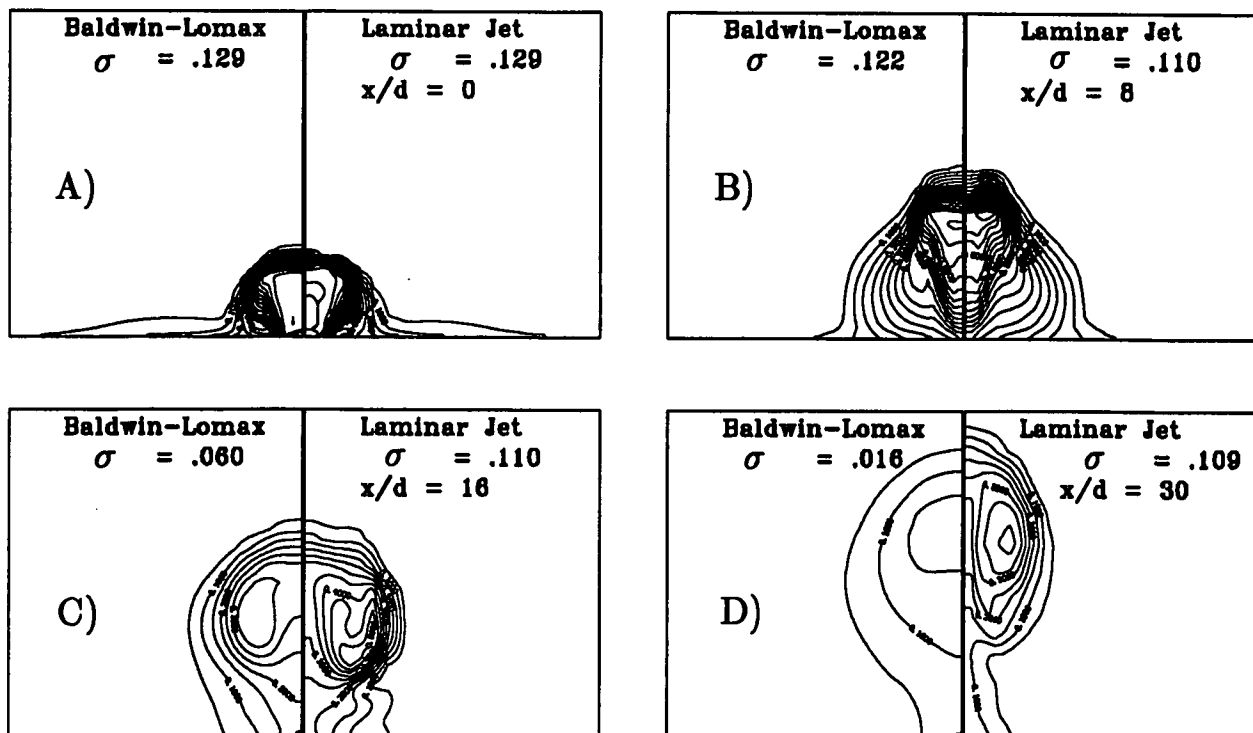


Figure 9. Comparison of mole fraction values at four crossflow planes between the Baldwin-Lomax and Laminar Jet solutions.

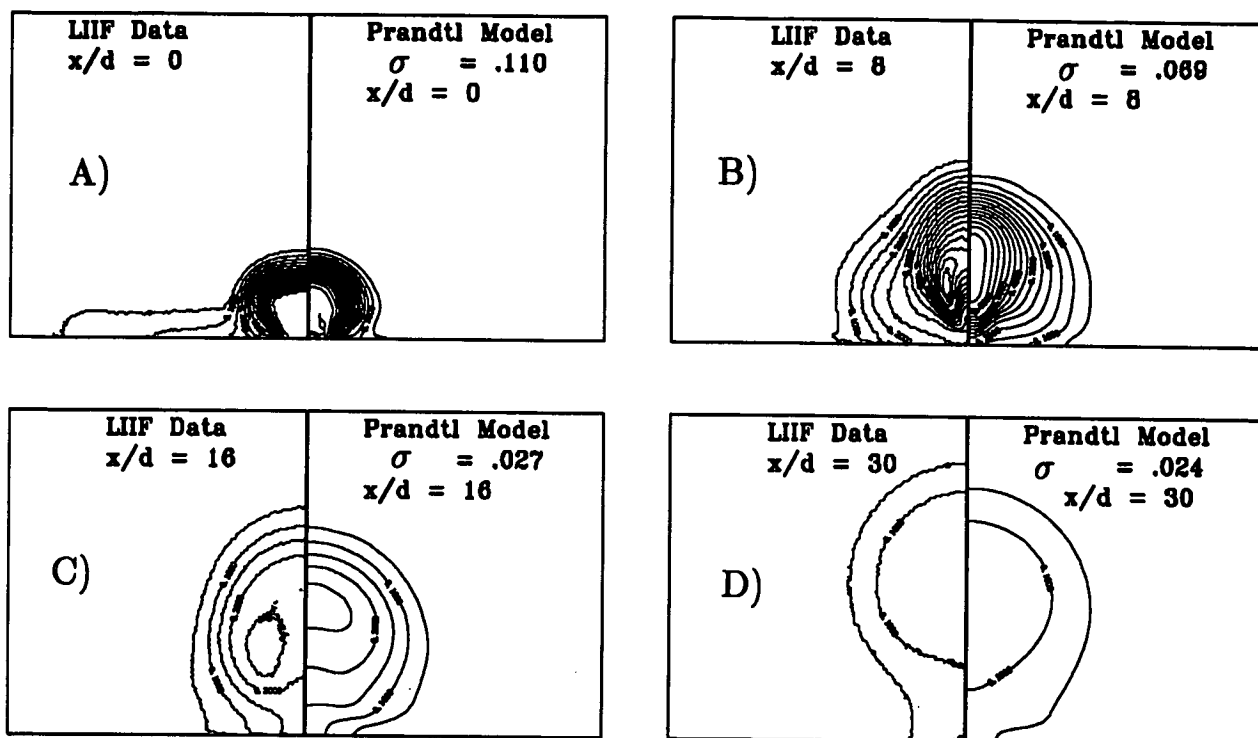


Figure 10. Comparison of mole fraction values at four crossflow planes between the measured and the Prandtl solutions.

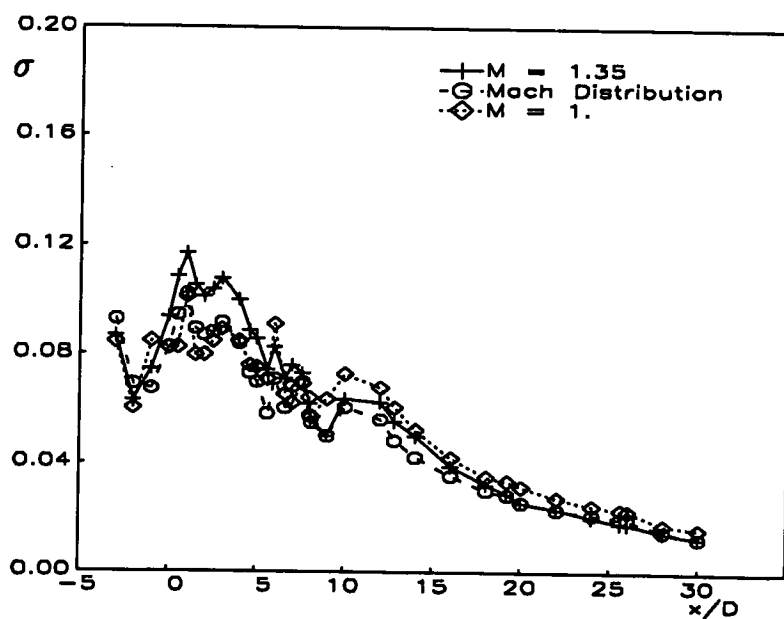


Figure 11. Standard deviation for solutions obtained with different jet exit conditions.